

Article

Improvement of the Corrosion Resistance by Addition of Ni in Lean Duplex Stainless Steels

Heon-Young Ha ^{*}, Tae-Ho Lee ^{*}, Sung-Dae Kim, Jae Hoon Jang  and Joonoh Moon

Ferrous Alloy Department, Korea Institute of Materials Science, Changwon 51508, Korea; sdkim@kims.re.kr (S.-D.K.); jhjang@kims.re.kr (J.H.J.); mjo99@kims.re.kr (J.M.)

^{*} Correspondence: hyha2007@kims.re.kr (H.-Y.H.); lth@kims.re.kr (T.-H.L.); Tel.: +82-55-280-3422 (H.-Y.H.); +82-55-280-3434 (T.-H.L.); Fax: +82-55-280-3599 (H.-Y.H. & T.-H.L.)

Received: 29 May 2020; Accepted: 3 July 2020; Published: 4 July 2020



Abstract: On newly developed Fe_{balance}-18Cr-7Mn-3Mo-3W-0.4N-(0.03, 0.57)Ni (in wt%) lean duplex stainless steels, the microstructure, element partitioning behavior, and resistance to pitting corrosion were investigated. After solution treatments, the two alloys were found to have similar microstructures in terms of phase fraction and grain size, and have a precipitation-free matrix. The polarization tests revealed that the addition of Ni was beneficial to improve the resistance to pitting corrosion, which was confirmed by the rise in pitting and repassivation potentials. The uniform corrosion behavior and galvanic corrosion rate of the matrix were investigated to explain the improved pitting corrosion resistance of the Ni-added lean duplex stainless steel. As a result, it was found that the addition of Ni enhanced the resistance to uniform corrosion by reducing the galvanic corrosion rate between the ferrite and austenite phases in the lean duplex stainless steel; thus, the pit growth rate was decreased, leading to improvement of the resistance to pitting corrosion.

Keywords: lean duplex stainless steel; pitting corrosion; galvanic corrosion; nickel

1. Introduction

Duplex stainless steels (DSSs) have a dual-phase structure composed of approximately equal amounts of ferrite (α) phase and austenite (γ). The DSSs possess good combination of mechanical and corrosion properties, and they are well known for excellent resistance to stress corrosion cracking in comparison with single-phase stainless steels (SSs) [1–10]. In addition, DSSs are economically attractive because commercial DSSs commonly contain only 1–7 wt% Ni, which is less than the Ni content of FeCrNi-based γ -SS (8–24 wt%) [2,6,9,11]. These advantages of DSSs make them promising alternatives to γ -SSs, and thus, demands for DSSs show a continuous increase in various industrial fields such as the on/off-shore oil and gas industry and chemical process industry [2,3,5,12–14].

Economic feasibility of DSSs can be further achieved by reducing the amount of expensive alloying elements, particularly Ni. Thus, various lean-DSSs (LDSSs), in which Ni is replaced with other γ stabilizers, such as Mn and N, have been developed and investigated [1,14–18]. Recently, this author group has proposed new LDSSs [17,19], which comprise 16.5–19.5 wt% Cr, 2.5–3.5 wt% Mo, 1.0–3.5 wt% W, 5.5–7.0 wt% Mn, 0.35–0.45 wt% N, and less than 0.7 wt% Ni with a remainder of Fe. The developed LDSSs are characterized by their excellent mechanical performances. The LDSSs are found to have the yield strengths of 574–635 MPa and the tensile strengths of 826–878 MPa, which are much higher than those of commercial γ -SSs, such as UNS S30400 and S31603, and even better than commercial DSSs, UNS S32304 and S31803. In addition, the LDSSs exhibit high elongation values of 40–51%, which are notable levels for general DSSs and comparable to commercial γ -SS. Moreover, it is revealed that the resistance to localized corrosion of the LDSSs is superior to that of UNS S31603 alloy. Thus, considering

the desirable combination of the mechanical and corrosion properties of the LDSSs, it can be concluded that the developed LDSSs have the potential to be applied to industrial field.

From an economical point of view, the use of Ni is intentionally limited for LDSSs as mentioned above. However, the authors have found that a small amount of Ni less than 1 wt% is useful to improve the localized corrosion resistance of LDSS, although Ni is generally known to have little effect on the pitting corrosion resistance in neutral NaCl solutions [20–22]. Thus, in this paper, Fe_{balance}-18Cr-7Mn-3Mo-3W-0.4N-based (in wt%) LDSSs with and without Ni were fabricated, and the microstructures, element partitioning, and the pitting corrosion resistance of the LDSSs were examined. Then, the role of alloying Ni in the resistance to pitting corrosion of the LDSSs was discussed.

2. Materials and Methods

In this study, Fe_{balance}-18Cr-7Mn-3Mo-3W-0.4N-based (in wt%) LDSSs containing different concentrations of Ni (0.03 and 0.57 wt%) were investigated. The Ni content needs to be adjusted to 0.6 wt% or less in order to prevent the solution treatment temperature from becoming too high. The detailed chemical compositions of the LDSSs, denoted as Ni03 and Ni57, are given in Table 1, which were measured using optical emission spectroscopy (QSN 750-II, PANalytical, Almelo, the Netherlands) and inductively coupled plasma atomic emission spectroscopy (Optima 8300DV, PerkinElmer, Waltham, MA, USA).

Table 1. Chemical compositions (in wt%) of the investigated alloys measured using optical emission spectroscopy and inductively coupled plasma atomic emission spectroscopy.

Alloy	Fe	Cr	Mo	W	Ni	Mn	N	C
Ni03	Balance	18.35 ± 0.032	2.98 ± 0.019	3.02 ± 0.035	0.03 ± 0.007	6.64 ± 0.031	0.42 ± 0.002	0.013 ± 0.002
Ni57	Balance	17.99 ± 0.027	2.94 ± 0.021	3.09 ± 0.036	0.57 ± 0.012	6.65 ± 0.026	0.42 ± 0.002	0.012 ± 0.002

The LDSS ingots of 10 kg were fabricated through pressurized induction melting (VIM 4 III-P, ALD Vacuum Technologies GmbH, Hanau, German) under an N₂ atmosphere. The ingots were homogenized at 1250 °C for 2 h and hot-rolled onto plates with a thickness of 4 mm, followed by water quenching. Then, the hot-rolled plates were solution-treated at 1100 and 1180 °C for 30 min, respectively, in order to obtain dual-phase structure with a phase fraction (α : γ) of approximately 1:1. The temperatures for the solution treatments were determined based on the diagrams of the equilibrium phase fraction versus temperature (Figure 1), which were calculated using Thermo-Calc software (version 2019a, database TCFE 9.0, Thermo-Calc Software, Stockholm, Sweden (KTH)).

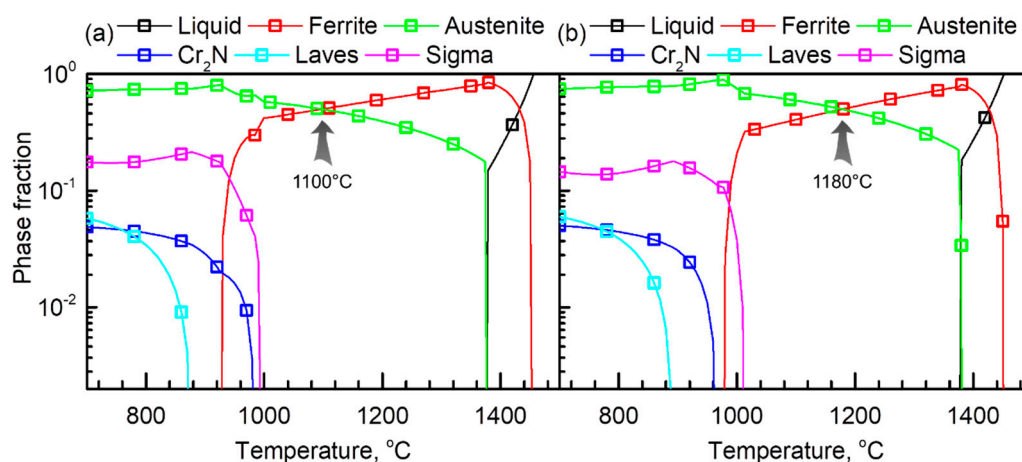


Figure 1. Equilibrium phase fractions of (a) Ni03 and (b) Ni57 alloys as a function of temperature calculated using Thermo-Calc software (version 2019a, TCFE 9.0 database).

Microstructures of the LDSSs were examined using a scanning electron microscope (SEM, IT-300, JEOL, Akishima, Japan) and electron backscatter diffraction (EBSD, HKL Nordlys Channel 5, Oxford Instruments, Abingdon, UK) in a SEM (JSM-7001F, JEOL, Akishima, Japan). For the SEM analyses, the LDSS specimens (10 mm × 10 mm × 4 mm) were polished using suspension with 1 µm-sized diamond particles, and chemically etched in an acid mixture (20 mL HNO₃ + 30 mL HCl + 50 mL deionized water) for 1–3 min. For the EBSD analyses, the specimens were polished using colloidal silica with a particle size of 0.02 µm. The EBSD analysis was performed on a scanning area 150 µm × 120 µm with a step size of 0.5 µm, and the grain boundaries were identified with the critical misorientation angle of 10°. From the EBSD images taken at 5 different locations, average values of the phase fractions (α : γ , in vol%) and grain sizes were measured. Then, the chemical compositions of the α and γ phases in the LDSSs were examined through an electron probe microanalysis (EPMA, SX100, CAMECA, Gennevilliers, France). For each alloy and each phase, 10 points were analyzed using the EPMA, and the average values were calculated.

Corrosion properties of the Ni03 and Ni57 alloys were evaluated through electrochemical tests. All of the electrochemical tests were performed using a three-electrode glass cell consisting of a saturated calomel reference electrode (SCE), a Pt plate counter electrode, and a specimen serving as a working electrode. For the working electrode, the LDSS specimens were mounted in cold epoxy resin and ground using SiC emery paper of up to 1500 grit. The exposed area for the test was controlled to be 0.2 cm² using electroplating tape. The tests were controlled by a potentiostat (Reference600+, GAMRY, Warminster, PA, USA).

The pitting corrosion resistance and repassivation tendencies of the LDSSs were evaluated through cyclic polarization tests in a 2 M NaCl solution at 40 °C. Based on our previous experiments, the LDSSs were immune to pitting corrosion, even in a 2 M NaCl solution at room temperature; thus, the polarization tests were performed in a 2 M NaCl solution and the solution temperature was controlled to be 40 °C. The specimens were immersed in the solution for 20 min prior to the potentiodynamic polarization tests for stabilization, from which the stable open circuit potential (OCP) was measured. After that, the potential was anodically increased from −0.1 V versus OCP to the potential at which the current density exceeded 0.1 mA cm^{−2}, and then, lowered to the repassivation potential (E_{rp}), with a potential sweep rate of 0.17 mV s^{−1}. Then, the dissolution rate after the stable pit formation was measured through potentiostatic tests. In the same condition (2 M NaCl solution at 40 °C), anodic constant potentials of 0.10 and 0.35 V_{SCE} were applied to the specimen for 20 min, and the current versus time curves were recorded.

For the two LDSSs, the sites for the pitting corrosion were observed using the SEM after immersion in a 2 M NaCl+1 M HCl solution at 40°C under the OCP for 30 min. The strong acid containing Cl[−] was needed for this experiment in order to simultaneously identify the phase boundary and the pit sites.

Uniform (or general) corrosion behavior of the LDSSs was examined through polarization tests in a 1 M HCl solution at 40 °C. After the OCP reached a steady state, the potential was scanned at a rate of 0.17 mV s^{−1} in the potential range for the active–passive transition. Then, the galvanic corrosion rate between the α and γ phases in the LDSS was quantified by measuring the corrosion depth between the two phases [10,17,23–25]. The polished specimens were immersed in a 1 M HCl solution at 40 °C, and after 20 min of immersion, the three-dimensional corroded morphology and the corrosion depth were examined using a surface optical profiler (Wyko NT8000, Veeco, Plainview, NY, USA). All of the potentiodynamic and potentiostatic tests were repeated at least five times for each specimen to verify reproducibility.

3. Results

3.1. Microstructure

Figure 1a,b show equilibrium fractions of the liquid, α , γ , Cr₂N, Laves, and sigma (σ) phase in the Ni03 and Ni57 alloys, respectively. In the two LDSSs, Cr₂N, Laves, and the σ phases are expected to

precipitate at below approximately 1000 °C, and the dual-phase without precipitates can be obtained in the temperature range between approximately 1000 and 1350 °C. In order to control the phase fraction (α : γ) to be 1:1, 1100 °C was determined for the solution treatment for the Ni03 alloy. On the other hand, the addition of Ni to the Ni03 alloy expands the temperature range for the stable γ , thus, the solution treatment temperature for the Ni57 was determined as 1180 °C.

Figure 2a,b exhibit SEM images of the microstructure solution-treated Ni03 and Ni57 alloys, respectively. After the solution treatment, the α and γ phases coexisted in both LDSSs, as shown in Figure 2(a-1),(b-1). The relatively light grey phase was the α phase and the dark grey phase with annealing twin was the γ phase, as marked in the SEM images. In addition, nonmetallic inclusions, which possibly act as initiation sites for localized corrosion [26–28], were rarely observed. The magnified SEM images (Figure 2(a-2),(b-2)) show that the precipitations, such as Cr_2N and σ , were not observed, even at the grain boundaries in both LDSSs.

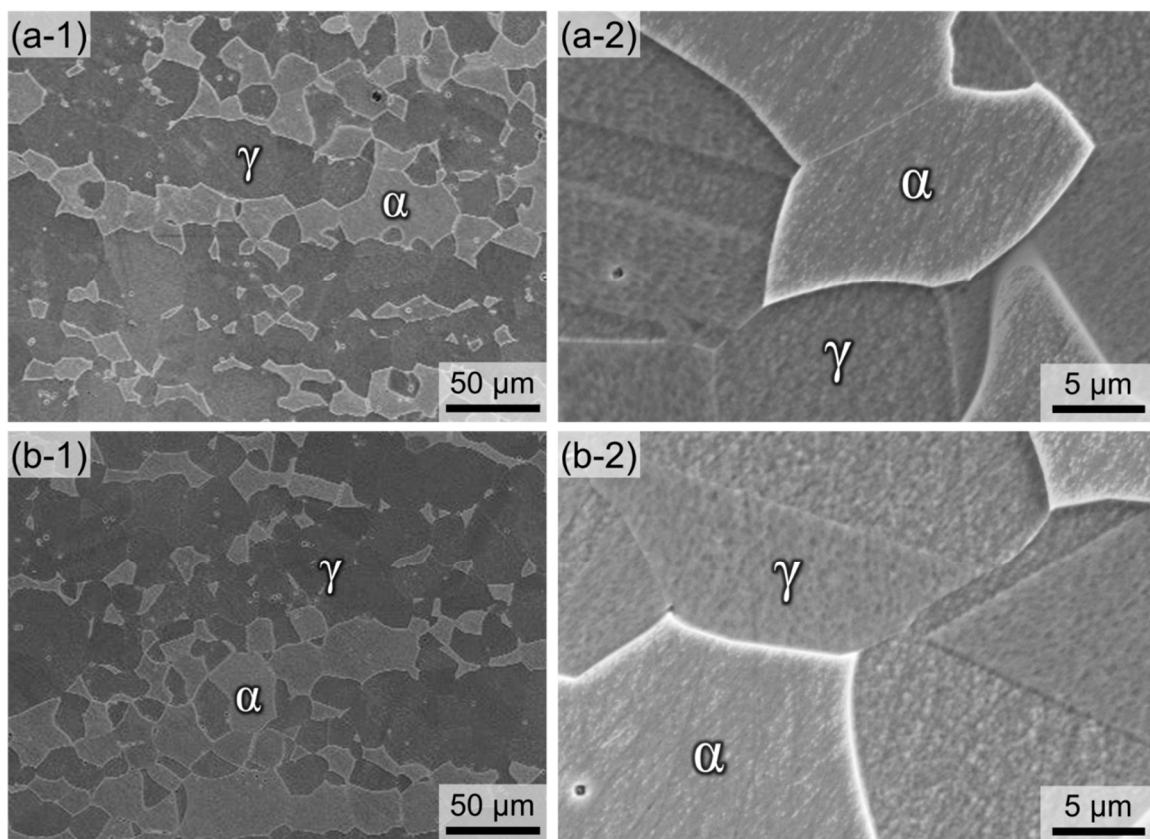


Figure 2. Microstructures of (a-1,a-2) Ni03 and (b-1,b-2) Ni57 alloys observed using a SEM taken at (a-1,b-1) low and (a-2,b-2) high magnifications.

The phase fraction and grain size were measured using EBSD analyses. Figure 3(a-1,b-1) are grey scale image quality maps of the Ni03 and Ni57 alloys, respectively, and Figure 3(a-2,b-2) are the corresponding phase maps of the LDSSs. The α phase fraction of the Ni03 alloy was measured to be 49.8 vol% and that of the Ni57 alloy was 48.4 vol%. The average grain sizes of the two LDSSs are presented in Table 2 and Figure 3c. The grain sizes of the α phases of the Ni03 and Ni57 alloys were 12.24 and 12.37 μm , respectively, and those of the γ phases were 9.87 and 10.88 μm for the Ni03 and Ni57 alloys, respectively. The two LDSSs were generally similar in grain sizes, but the Ni57 alloy had marginally larger grain in comparison with that of the Ni03 alloy, which was due to the higher solution treatment temperature for the Ni57 alloy.

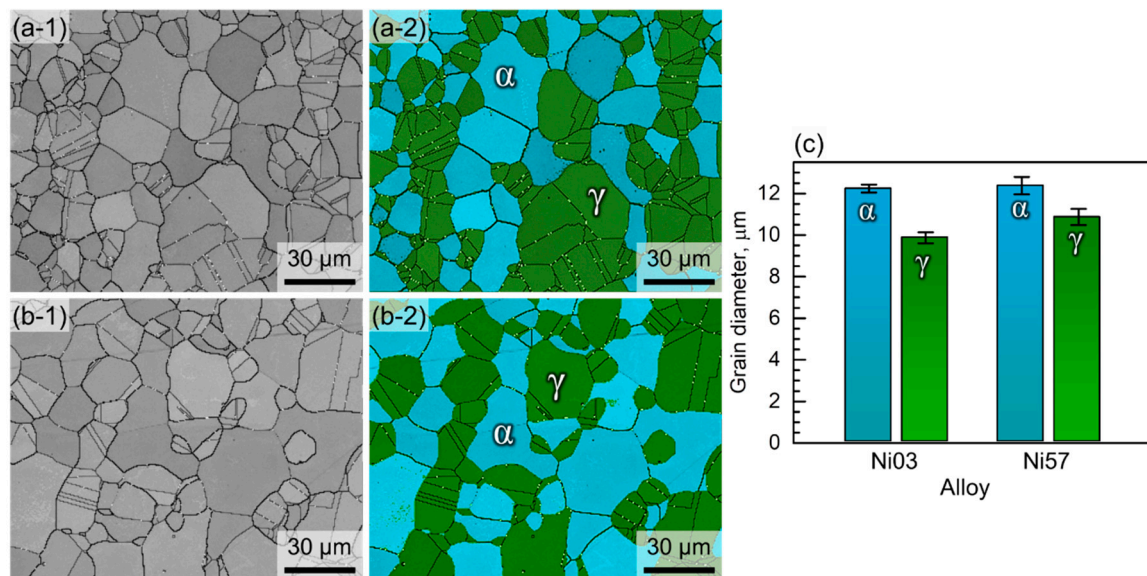


Figure 3. EBSD image quality maps of (a-1) Ni03 and (b-1) Ni57 alloys and phase maps of (a-2) Ni03 and (b-2) Ni57 alloys (green—face-centered cubic (γ) and blue—body centered cubic (α)). (c) Grain diameters of the α and γ phases in the Ni03 and Ni57 alloys.

Table 2. Chemical compositions (in wt %) of the α and γ phases of the Ni03 and Ni57 alloys measured using an EPMA.

Alloy	Phase	Grain Diameter, μm	Concentration, wt%							
			Fe	Cr	Mo	W	Mn	N	Ni	PREN
Ni03	α	12.24 ± 0.19	Balance	17.945 ± 0.078	3.628 ± 0.041	3.814 ± 0.039	6.157 ± 0.047	0.022 ± 0.009	0.041 ± 0.017	30.406
	γ	9.87 ± 0.26		18.674 ± 0.063	2.122 ± 0.065	2.452 ± 0.027	7.233 ± 0.063	0.690 ± 0.017	0.021 ± 0.006	33.529
Ni57	α	12.37 ± 0.42	Balance	17.723 ± 0.064	3.506 ± 0.044	3.820 ± 0.027	6.108 ± 0.079	0.015 ± 0.006	0.423 ± 0.020	29.728
	γ	10.88 ± 0.39		18.202 ± 0.057	2.269 ± 0.053	2.449 ± 0.031	7.120 ± 0.072	0.659 ± 0.039	0.679 ± 0.036	33.155

$$\text{PREN} = [\text{Cr}] + 3.3 \times [\text{Mo}] + 1.65 \times [\text{W}] + 16 \times [\text{N}] - [\text{Mn}], \text{ in wt\%}$$

3.2. Alloying Element Partitioning

Table 2 and Figure 4 show the chemical compositions of the α and γ phases of the Ni03 and Ni57 alloys, which were examined using the EPMA. After the solution treatment, the concentrations of Mo (Figure 4b) and W (Figure 4c), the α stabilizer, are higher in the α phase than in the γ phase by approximately 1.5 wt%. As for another α stabilizer, the partitioning behavior of Cr in the Ni03 and Ni57 alloys was noticeable (Figure 4a). The Cr content in the bulk matrix of the Ni57 alloy was lower than that of the Ni03 alloy, thus, the difference in the Cr content between the two LDSSs was shown in Figure 4a. The notable point is that the γ phases in both Ni03 and Ni57 alloys contain higher Cr than the α phases, although Cr is the α stabilizer. A similar result can be found in the N-bearing DSSs ($\text{Fe}_{\text{balance}}\text{-18Cr-6Mn-3Mo-0.4N-(2.13, 5.27)W}$, in wt%) [17]. A high concentration of Cr in the γ phase is presumably due to the strong affinity between N and Cr. The Cr-partitioning behavior is slightly affected by the Ni addition to the matrix, that is, the difference in the Cr concentrations between the α and γ phases of the Ni03 alloy was 0.73 wt% and that of the Ni57 alloy was decreased to 0.48 wt%. As for the γ stabilizers, Mn (Figure 4d), N (Figure 4e), and Ni (Figure 4f) were enriched in the γ phases in both DSSs, and the partitioning of Mn and N was hardly affected by the presence of Ni in the Ni03 matrix, as shown in Figure 4d,e. Lastly, the partitioning of Ni was shown in Figure 4f. The γ phase of the Ni57 alloy contained 0.68 wt% Ni, while the α phase has only 0.42 wt% Ni.

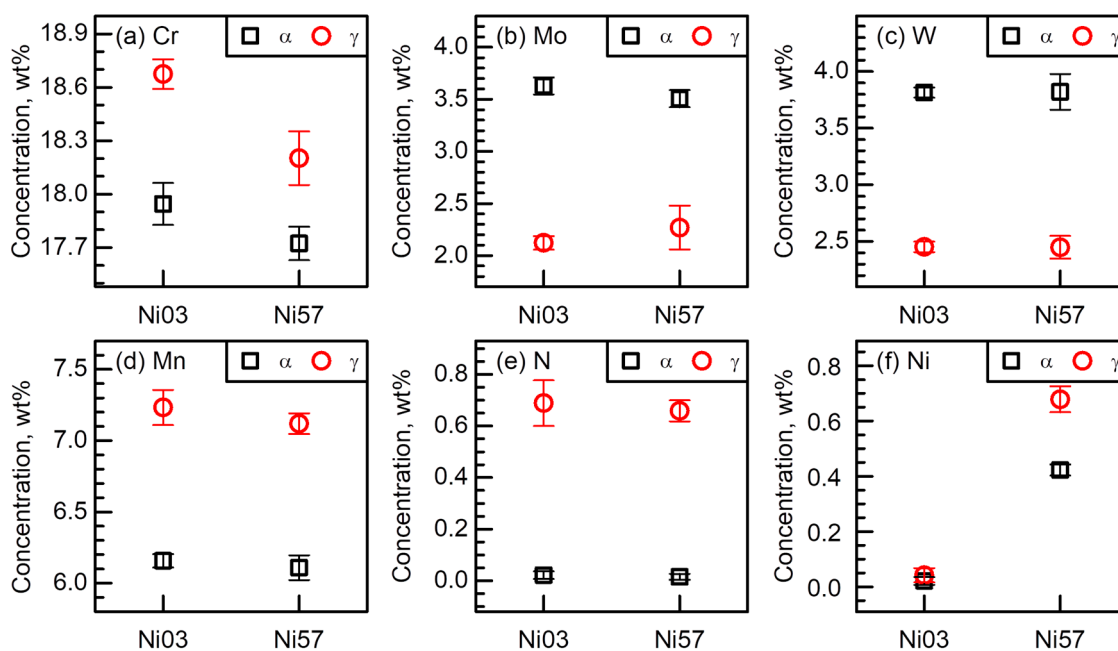


Figure 4. Chemical compositions of (a) Cr (b) Mo, (c) W, (d) Mn, (e) N, and (f) Ni of the α and γ phases in the Ni03 and Ni57 alloys measured using the EPMA.

3.3. Pitting Corrosion Behavior

The resistance to pitting corrosion of the LDSSs was assessed through cyclic potentiodynamic polarization tests. From the repeatedly obtained polarization curves, three representative results for each LDSS were presented in Figure 5, verifying reproducibility. From the polarization tests, pitting potential (E_{pit}) and E_{rp} could be obtained, and the average values of E_{pit} and E_{rp} were plotted in Figure 5c as a function of the Ni content ($[Ni]$).

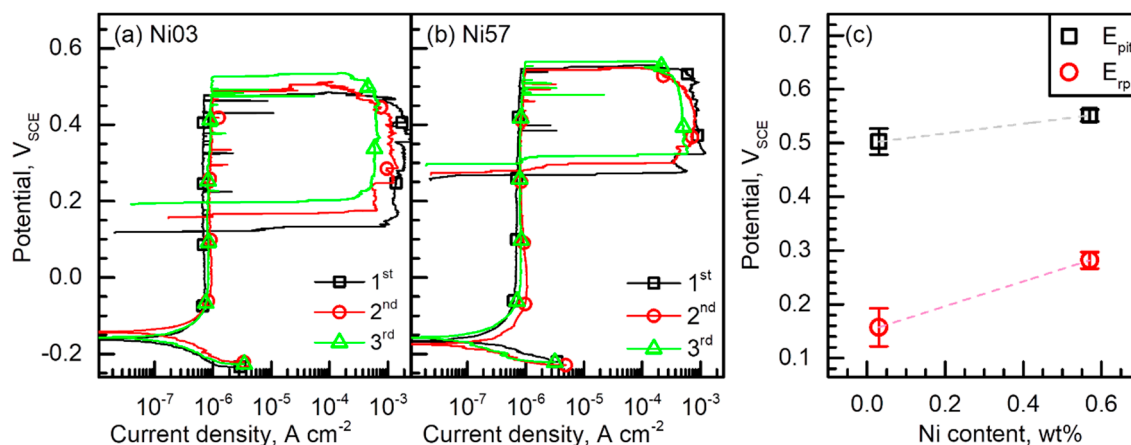


Figure 5. Repeatedly measured cyclic potentiodynamic polarization curves of (a) Ni03 and (b) Ni57 alloys. The polarization tests were obtained in 2 M NaCl at 40 °C with a potential sweep rate of 0.17 mV s⁻¹. (c) Average pitting potential (E_{pit}) and repassivation potential (E_{rp}) of the alloys.

Corrosion potential (E_{corr}) of the Ni03 and Ni57 alloys were -0.151 and -0.158 V_{SCE}, respectively, and both LDSSs were in passive state at their E_{corr} levels. Comparing Figure 5a,b, it is obvious that the Ni addition changed both E_{pit} and E_{rp} (Figure 5). The average E_{pit} of the Ni03 and Ni57 alloys were 0.503 and 0.551 V_{SCE}, respectively, and the average E_{rp} of the two alloys were 0.157 and 0.282 V_{SCE}, respectively. Thus, the slope of E_{pit} versus $[Ni]$ graph ($\Delta E_{pit}/\Delta[Ni]$) was 0.090 V wt%⁻¹ and that of the E_{rp} versus $[Ni]$ graph ($\Delta E_{rp}/\Delta[Ni]$) was 0.231 V wt%⁻¹. It was shown that the addition of only 0.57 wt%

Ni increased both E_{pit} and E_{rp} , and note that the beneficial effects of Ni were more pronounced in increasing E_{rp} . In addition, it was also noted that the size of the cyclic polarization loop and the maximum current density were affected by the Ni addition. The maximum dissolution current density of the Ni03 alloy was 1.228 mA cm^{-2} and that of the Ni57 alloy was 0.687 mA cm^{-2} , on average. This observation is considered to be the reason for the higher value of $\Delta E_{\text{rp}}/\Delta[\text{Ni}]$ than the $\Delta E_{\text{pit}}/\Delta[\text{Ni}]$.

The increase in the current densities after the stable pit formation of the Ni03 and Ni57 alloys could be compared more clearly by Figure 6. Figure 6a exhibits the representative polarization curves of the Ni03 and Ni57 alloys chosen from Figure 5, and Figure 6b,c are the current–time curves as a result of potentiostatic tests on the two alloys. The potentiostatic tests were conducted in the same condition for the potentiodynamic polarization tests, that is a 2 M NaCl solution at 40°C , and the applied potentials were $0.35 V_{\text{SCE}}$ (Figure 6b) and $0.10 V_{\text{SCE}}$ (Figure 6c). Under the anodic polarization at $0.10 V_{\text{SCE}}$ (Figure 6c), which was lower than the E_{rp} of the two LDSSs, both alloys were passivated and a few current spikes indicating metastable pitting corrosion were observed in the current–time curves. On the other hand, applying $0.35 V_{\text{SCE}}$ caused a stable pitting corrosion, that is, the initial passivation for a few seconds was followed by a continuous and irreversible increase in the current density (Figure 6b). Note that the current increase rate (i.e., $\Delta\text{current}/\Delta\text{time}$) was faster in the Ni03 alloy than in the Ni57 alloy. It took approximately 500 s for the Ni03 alloy to reach the dissolution current of $500 \mu\text{A}$, but for the Ni57 alloy, it needed approximately 1200 s.

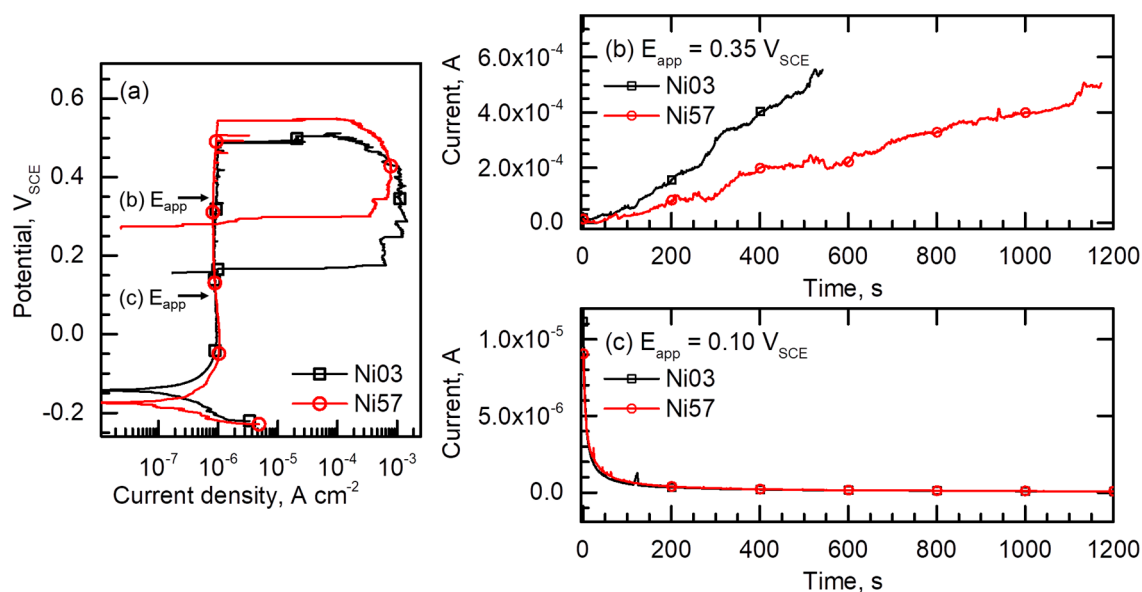


Figure 6. (a) Representative cyclic potentiodynamic polarization curves of the Ni03 and Ni57 alloys chosen from Figure 5a,b. Current–time curves of the Ni03 and Ni57 alloys obtained from potentiostatic tests measured in a 2 M NaCl solution at 40°C under constant applied potentials (E_{app}) of (b) $0.35 V_{\text{SCE}}$ and (c) $0.10 V_{\text{SCE}}$.

Then, the initiation sites for the pitting corrosion were examined. The Ni03 and Ni57 specimens were immersed in a 1 M HCl + 2 M NaCl solution at 40°C , and after 30 min of immersion, pitting corrosion occurred in both alloys. Figure 7a,b exhibit the pit morphologies of the Ni03 and Ni57 alloys, respectively. The stable pits, with a size of several μm , were observed at the γ side of the phase boundary for both DSSs.

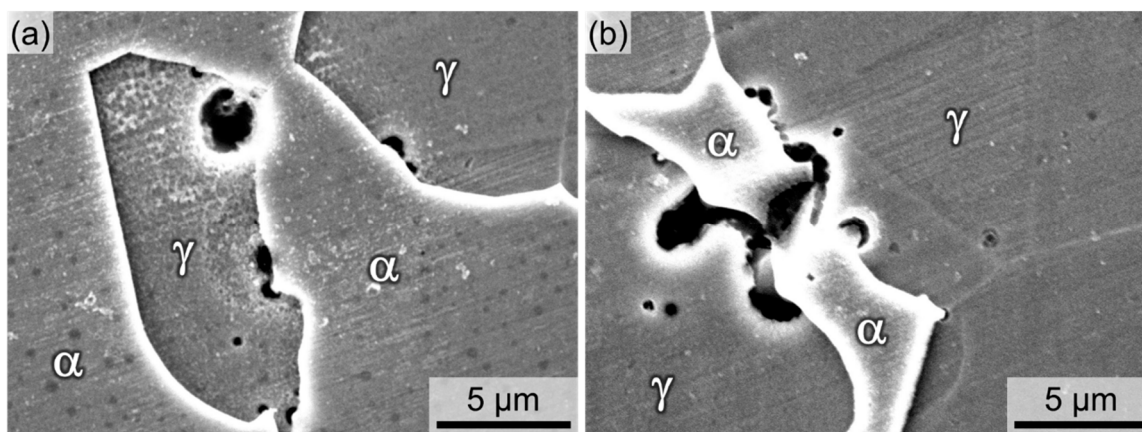


Figure 7. Pit morphologies of (a) Ni03 and (b) Ni57 alloys after immersion in a 1 M HCl + 2 M NaCl solution at 40 °C for 30 min.

3.4. Uniform Corrosion Behavior

Once a passive film is broken forming a pit embryo, the electrolyte confined in the pit cavity becomes acidified as the pit grows because of the hydrolysis reaction during the metal dissolution [29,30]. In the pit cavity, uniform dissolution begins to occur on the metal surface exposed to the acidified solution without passive film, and the uniform dissolution rate of metal determines the pit growth rate. Therefore, in order to compare the pit growth rates of the Ni03 and Ni57 alloys, the matrix dissolution rates were examined in the acidified chloride solution, simulating the electrolyte in the pit cavity.

Figure 8a shows the polarization behavior of the Ni03 and Ni57 alloys measured in a 1 M HCl solution at 40 °C. In the strong acid, the two alloys exhibit typical active–passive transition during the anodic polarization. E_{corr} of the Ni03 and Ni57 alloys were -0.485 and -0.448 V_{SCE}, respectively, confirming that the Ni addition increases the nobility of the Ni03 matrix. From Figure 8a, the corrosion rate (i_{corr}) and critical current density (i_{crit}) were measured and the values were shown in Figure 8b. i_{corr} values of the Ni03 and Ni57 alloys were 0.754 and 0.486 mA cm⁻², respectively, and i_{crit} values of the two alloys were 3.362 and 1.244 mA cm⁻², respectively.

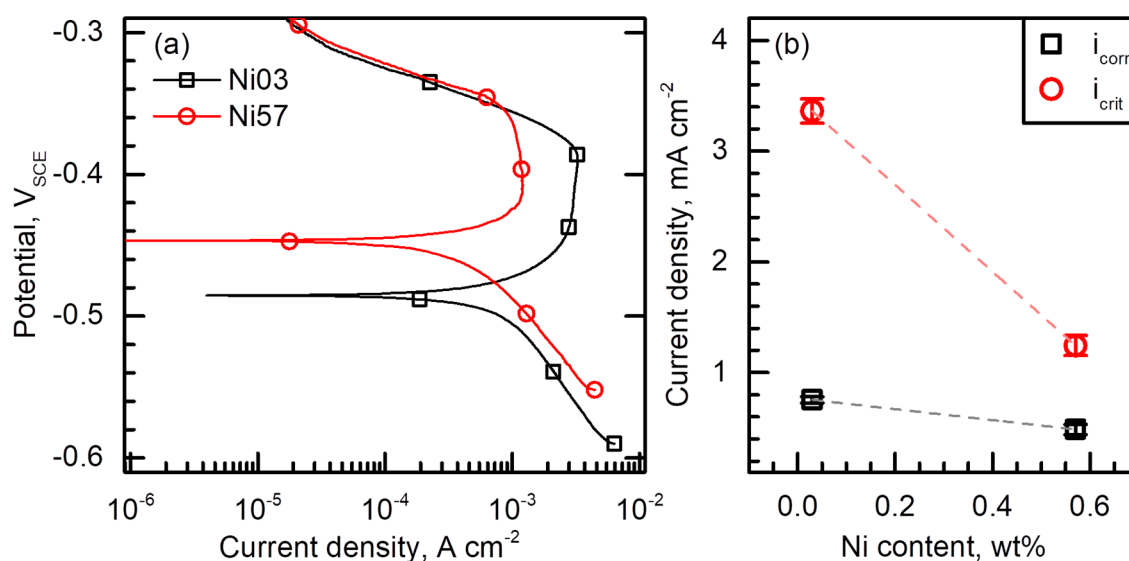


Figure 8. (a) Potentiodynamic polarization curves of the Ni03 and Ni57 alloys measured in a 1 M HCl solution at 40 °C with a potential sweep rate of 0.17 mV s⁻¹. (b) Corrosion rate (i_{corr}) and critical anodic current density (i_{crit}) of the alloys.

3.5. Galvanic Corrosion Behavior

The uniform dissolution rate of the LDSS matrix is inevitably related to the galvanic corrosion rate between the α and γ phases. Thus, for the Ni03 and Ni57 alloys, the galvanic corrosion rates between the α and γ phases were quantified by the measuring corrosion depth between the two phases. For this, the LDSS specimens were immersed in a 1 M HCl solution at 40 °C, and the corrosion morphologies were examined using a surface profiler.

Figure 9(a-1,b-1) show three-dimensional topographic maps of the corroded Ni03 and Ni57 specimens, respectively, after immersion in the HCl solution. It is shown that the two constituent phases are different in corrosion rate in this strong acid solution. In both alloys, the more corroded phase (the blue phase) was the γ phase, which was confirmed by the annealing twins. Then, the dissolution depth of the active phase (γ , in this case) relative to the noble phase (α) could be measured from Figure 9(a-2,b-2). Analyses on the contour maps revealed that the average corrosion depths of the γ phase relative to that of the α were 0.51 and 0.34 μm for the Ni03 (Figure 9(a-3)) and Ni57 alloys (Figure 9(b-3)), respectively. Thus, Figure 9 indicates that the addition Ni to the Ni03 alloy decreased the galvanic corrosion rate between the γ and α phases.

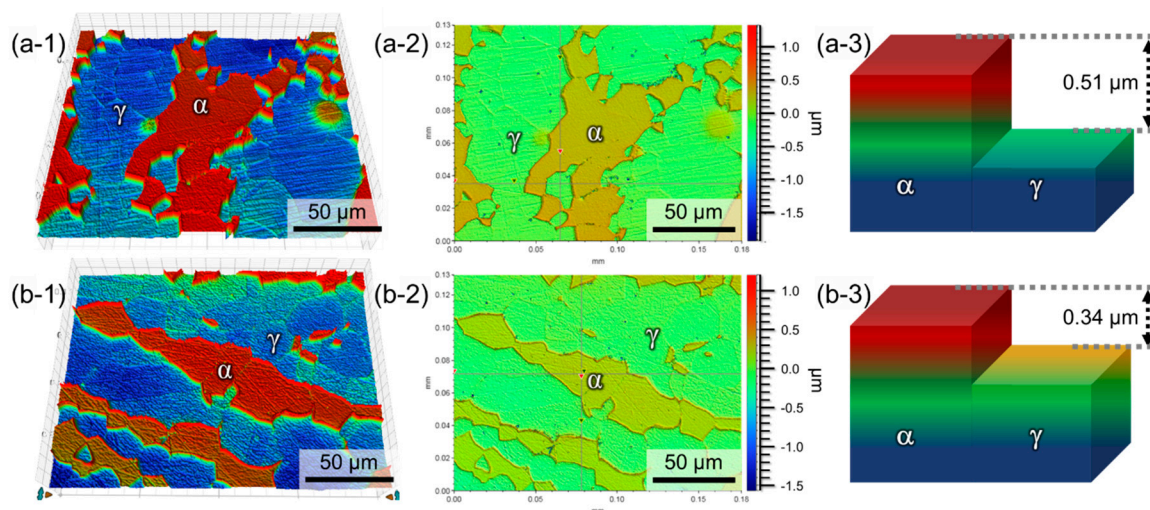


Figure 9. Three-dimensional topographs of the corroded surfaces of (a-1) Ni03 and (b-1) Ni57 alloys, and contour maps with a color scale bar of (a-2) Ni03 and (b-2) Ni57 alloys. The images were obtained after immersion in a 1 M HCl solution at 40 °C for 20 min. Schematic diagram of the corrosion depths of (a-3) Ni03 and (b-3) Ni57 alloys.

4. Discussion

In the present paper, the Fe_{balance}-18Cr-7Mn-3Mo-3W-0.4N-(0.03, 0.57)Ni (in wt%) LDSSs were carefully fabricated and solution-treated. As shown in Figures 2 and 3, the two alloys exhibited similar microstructural characteristics, in terms of the grain size and the phase fraction. In addition, the second phases, such as Cr₂N and σ , were not observed in both LDSSs after the solution treatment. Figure 4 and Table 2 exhibited alloying element partitioning behavior into the α and γ phases in both LDSSs. It was shown that the Ni addition to the bulk Ni03 matrix had negligible effect on the partitioning behavior of Mo, W, Mn, and N, and the difference in Cr concentrations between the α and γ phases was slightly reduced in the Ni57 alloy comparing with the Ni03 alloy. In addition, Ni was preferentially partitioned into the γ phase of the Ni57 alloy. The microstructural analyses suggested that the corrosion behavior of the Ni03 and Ni57 alloys were primarily affected by the chemical compositions of the constituent phases.

The pitting corrosion resistance of the two LDSSs was assessed by measuring the E_{pit} and E_{rp} through the polarization tests in a 2 M NaCl solution at 40 °C. Figure 5 indicated that the Ni addition to the Ni03 alloy increased both E_{pit} and E_{rp} , and the positive effect of Ni was more pronounced in the

increase in E_{rp} . Since higher E_{pit} indicates higher resistance to the stable pit formation, and higher E_{rp} means greater tendency for the pit extinction (i.e., repassivation), Figure 5 demonstrated that the Ni57 alloy possessed better resistance to pitting corrosion than the Ni03 alloy. In addition, it was also shown that the Ni addition reduced the size of the loop in the cyclic polarization curve, which implied that the alloying Ni retarded the pit growth rate. This observation was confirmed again by the measurement of the dissolution current after stable pit initiation of the two LDSSs (Figure 6b).

The uniform corrosion rate of the matrix has a strong correlation with the pit growth rate, and the uniform corrosion of dual-phase steel inside the pit is accompanied by the galvanic corrosion between the two phases. Thus, the uniform and galvanic dissolution rates between the two constituent phases were measured in the simulated solution inside the pit, that is, the acidified chloride solution, through the polarization tests (Figure 8) and immersion tests (Figure 9).

The polarization curves obtained in a 1 M HCl solution at 40 °C (Figure 8) indicated that the Ni addition to the Ni03 matrix enhanced the resistance to uniform corrosion, which was confirmed by reduced i_{corr} and i_{crit} , and increased E_{corr} . That is, the dissolution rate of the Ni03 alloy in a strong acid containing chloride ions was faster than that of the Ni57 alloy under anodic polarization as well as under open circuit conditions. In addition, it was noted that the decrease in i_{crit} more sensitively depended on the [Ni] than i_{corr} , as shown in Figure 8b. During the pit growth, the matrix inside the pit cavity exposed to the acidified chloride solution behaves as a local anode and the metal surface around the pit mouth behaves as a local cathode. Thus, in the pit cavity, active dissolution of the matrix under anodic polarization continues until the onset of the repassivation. For this reason, the significant decrease in the i_{crit} by the addition of Ni (Figure 8b) implied that the pit growth rate was slowed down by the addition of Ni, which consequently assisted repassivation of both stable and metastable pits. Therefore, Figure 8b well explained the results from Figure 5c, that is, the Ni addition retarded the dissolution of the Ni03 matrix and consequently, increased the both E_{pit} and E_{rp} .

The reduced i_{corr} was found to be due to the suppressed galvanic corrosion rate between the α and γ phases (Figure 9). From Figure 9, it was firstly noted that dissolution rates of the γ and α phases were different, and the γ phase was the more active phase than the α phase. Nobility of the α and γ phases is determined by the chemical composition. The EPMA analysis results (Figure 4) showed that the γ phases of both LDSSs contained higher Cr, Mn, and N concentrations than the α phase, and Cr and Mn are thermodynamically and galvanically more active than Fe. In addition, alloying N is reported to decrease the nobility of the FeCr-based alloy [31]. Thus, the γ phase enriched with Cr, Mn, and N in the LDSSs dissolved more preferentially when it was in contact with the nobler phase, α . For the Ni57 alloy, the added Ni was partitioned into the two phases, and the γ phase contained 0.68 wt% Ni, while the α phase had only 0.42 wt% Ni. Still, the γ phase of the Ni57 alloy was the relatively more active phase, but the Ni addition changed the corrosion depth. Thus, Figure 9 secondly indicated that the enrichment of Ni in the γ phase of the Ni57 alloy resulted in reducing the dissolution rate of γ galvanically coupled with the α . The decreased galvanic corrosion rate of the Ni57 alloy showed a good agreement with the reduced i_{corr} value of the Ni57 alloy shown in Figure 8.

Consequently, the reduced galvanic corrosion rate between the α and γ phases and the increased resistance to uniform corrosion of the Ni57 alloy implied the decrease in the growth rate of the pit cavity, which was responsible for the increase in the potentials for the stable pit initiation (i.e., E_{pit}) and the pit extinction (i.e., E_{rp}) to the higher values accordingly.

The present study strongly suggests that controlling the galvanic corrosion rate between the constituent phases for DSSs is helpful to improve the resistance to pitting corrosion, and one of the effective ways to achieve the favorable resistance to pitting corrosion for the LDSS would be the use of small amount of Ni. The findings of this paper could be extended to other similar alloy systems.

5. Conclusions

In the present paper, LDSSs with a composition of $Fe_{balance-18Cr-7Mn-3Mo-3W-0.4N-(0.03, 0.57)Ni}$ (in wt%) were carefully fabricated and solution-treated. For the LDSSs, the microstructures, element

partitioning, and the resistance to pitting corrosion were examined. Based on the results, the following conclusions could be drawn.

(1) The two alloys were found to have similar microstructures in terms of phase fraction and grain size, and to have a precipitation-free matrix. The composition analyses results suggested that the Ni addition to the Ni03 matrix had a negligible effect on the partitioning behavior of Cr, Mo, W, Mn, and N. Only Ni was preferentially partitioned into the γ phase of the Ni57 alloy. Thus it was found that the corrosion behavior of the Ni03 and Ni57 alloys were primarily affected by the chemical compositions of the constituent phases.

(2) The polarization tests in a NaCl solution revealed that the addition of Ni was beneficial to improve the resistance to pitting corrosion, which was confirmed by increased E_{pit} and E_{rp} , and the positive effect of Ni was more pronounced in the increase in E_{rp} . In addition, it was found that the Ni addition decreased the pit growth rate.

(3) The uniform corrosion behavior and galvanic dissolution rates between the two constituent phases were measured in the acidified chloride solution. As a result, it was shown that the Ni addition to the Ni03 matrix improved the resistance to uniform corrosion, and decreased the galvanic corrosion rate between the γ and α phases, thus, the pit growth rate was decreased leading to improvement of the resistance to pitting corrosion.

Author Contributions: Conceptualization, H.-Y.H. and T.-H.L.; methodology, H.-Y.H. and T.-H.L.; software, J.H.J.; validation, S.-D.K., J.H.J., and J.M.; investigation, S.-D.K., J.M., and H.-Y.H.; writing—original draft preparation, H.-Y.H. and S.-D.K.; writing—review and editing, T.-H.L.; funding acquisition, H.-Y.H. All authors have read and agreed to the published version of the manuscript.

Funding: This study was supported by the Basic Science Research Program of the National Research Foundation (NRF), funded by the Ministry of Science & ICT (NRF-2019R1C1C1010246) and the Ministry of Trade, Industry & Energy (MI, Korea) under Strategic Core Materials Technology Development Program (No. 10067375).

Conflicts of Interest: The authors declare no conflict of interest.

References

1. Lo, K.H.; Shek, C.H.; Lai, J.K.L. Recent developments in stainless steels. *Mater. Sci. Eng. R* **2009**, *65*, 39–104. [[CrossRef](#)]
2. Chail, G.; Kangas, P. Super and hyper duplex stainless steels: Structures, properties and applications. *Procedia Struct. Integr.* **2016**, *2*, 1755–1762. [[CrossRef](#)]
3. Ornek, C.; Engelberg, D.L. Towards understanding the effect of deformation mode on stress corrosion cracking susceptibility of grade 2205 duplex stainless steel. *Mater. Sci. Eng. A* **2016**, *666*, 269–279. [[CrossRef](#)]
4. Rossi, B. Discussion on the use of stainless steel in constructions in view of sustainability. *Thin Walled Struct.* **2014**, *83*, 182–189. [[CrossRef](#)]
5. Santos, T.F.A.; Torres, E.A.; Lippold, J.C.; Ramirez, A.J. Detailed Microstructural Characterization and Restoration Mechanisms of Duplex and Superduplex Stainless Steel Friction-Stir-Welded Joints. *J. Mater. Eng. Perform.* **2016**, *25*, 5173–5188. [[CrossRef](#)]
6. Boillot, P.; Peultier, J. Use of Stainless Steels in the Industry: Recent and Future Developments. *Procedia Eng.* **2014**, *83*, 309–321. [[CrossRef](#)]
7. Knyazeva, M.; Pohl, M. Duplex steels: Part I: Genesis, formation, structure. *Metallogr. Microstruct. Anal.* **2013**, *2*, 113–121. [[CrossRef](#)]
8. Mohammed, G.R.; Ishak, M.; Aqida, S.N.; Abdulhadi, H.A. Effects of Heat Input on Microstructure, Corrosion and Mechanical Characteristics of Welded Austenitic and Duplex Stainless Steels: A Review. *Metals* **2017**, *7*, 39. [[CrossRef](#)]
9. Vannevik, H.; Nilsson, J.-O.; Frodigh, J.; Kangas, P. Effect of elemental partitioning on pitting resistance of high nitrogen duplex stainless steels. *ISIJ Int.* **1996**, *36*, 807–812. [[CrossRef](#)]
10. Ha, H.-Y.; Lee, T.-H.; Lee, C.-G.; Yoon, H. Understanding the relation between pitting corrosion resistance and phase fraction of S32101 duplex stainless steel. *Corros. Sci.* **2019**, *149*, 226–235. [[CrossRef](#)]

11. He, L.; Wirian, L.; Singh, P.M. Effects of Isothermal Aging on the Microstructure Evolution and Pitting Corrosion Resistance of Lean Duplex Stainless Steel UNS S32003. *Metall. Mater. Trans. A* **2019**, *50*, 2103–2113. [[CrossRef](#)]
12. Baddoo, N.R. Stainless steel in construction: A review of research, applications, challenges and opportunities. *J. Constr. Steel Res.* **2008**, *64*, 1199–1206. [[CrossRef](#)]
13. Kang, D.H.; Lee, H.W. Study of the correlation between pitting corrosion and the component ratio of the dual phase in duplex stainless steel welds. *Corros. Sci.* **2013**, *74*, 396–407. [[CrossRef](#)]
14. Zhao, Y.; Zhang, W.; Liu, Z.; Wang, G. Development of an easy-deformable Cr21 lean duplex stainless steel and the effect of heat treatment on its deformation mechanism. *Mater. Sci. Eng. A* **2017**, *702*, 279–288. [[CrossRef](#)]
15. Choi, J.Y.; Ji, J.H.; Hwang, S.W.; Park, K.-T. Strain induced martensitic transformation of Fe–20Cr–5Mn–0.2Ni duplex stainless steel during cold rolling: Effects of nitrogen addition. *Mater. Sci. Eng. A* **2011**, *528*, 6012–6019. [[CrossRef](#)]
16. Guo, Y.; Sun, T.; Hu, J.; Jiang, Y.; Jiang, L.; Li, J. Microstructure evolution and pitting corrosion resistance of the Gleeble-simulated heat-affected zone of a newly developed lean duplex stainless steel 2002. *J. Alloy. Compd.* **2016**, *658*, 1031–1040. [[CrossRef](#)]
17. Ha, H.-Y.; Lee, T.-H.; Kim, S. Effect of W on Stress Corrosion Cracking Susceptibility of Newly Developed Ni-Saving Duplex Stainless Steels. *Met. Mater. Int.* **2017**, *23*, 115–125. [[CrossRef](#)]
18. Ha, H.-Y.; Lee, C.-H.; Lee, T.-H.; Kim, S. Effects of Nitrogen and Tensile Direction on Stress Corrosion Cracking Susceptibility of Ni-Free FeCrMnC-Based Duplex Stainless Steels. *Materials* **2017**, *10*, 294. [[CrossRef](#)]
19. Ha, H.-Y.; Lee, T.-H.; Hwang, B.C. High-Performance High-Nitrogen Duplex Stainless Steels Excellent in Pitting Corrosion Resistance. U.S. Patent 9,663,850, 30 May 2017.
20. Ha, H.-Y.; Lee, T.-H.; Kim, S.-J. Synergistic effect of Ni and N on improvement of pitting corrosion resistance of high nitrogen stainless steels. *Corros. Eng. Sci. Technol.* **2014**, *49*, 82–86. [[CrossRef](#)]
21. Azuma, S.; Kudo, T.; Miyuki, H.; Yamashita, M.; Uchida, H. Effect of nickel alloying on crevice corrosion resistance of stainless steels. *Corros. Sci.* **2004**, *46*, 2265–2280. [[CrossRef](#)]
22. Yoon, Y.-S.; Ha, H.-Y.; Lee, T.-H.; Kim, S. Comparative study of stress corrosion cracking susceptibility of Fe18Cr10Mn- and Fe18Cr10Mn1Ni-based high nitrogen stainless steels. *Corros. Sci.* **2014**, *88*, 337–348. [[CrossRef](#)]
23. Ha, H.-Y.; Jang, M.-H.; Lee, T.-H.; Moon, J. Interpretation of the relation between ferrite fraction and pitting corrosion resistance of commercial 2205 duplex stainless steel. *Corros. Sci.* **2014**, *89*, 154–162. [[CrossRef](#)]
24. Ha, H.-Y.; Jang, M.-H.; Lee, T.-H.; Moon, J. Understanding the relation between phase fraction and pitting corrosion resistance of UNS S32750 stainless steel. *Mater. Charact.* **2015**, *106*, 338–345. [[CrossRef](#)]
25. Yoon, H.; Ha, H.-Y.; Lee, T.-H.; Kim, S.-D.; Jang, J.H.; Moon, J.; Kang, N. Pitting Corrosion Resistance and Repassivation Behavior of C-Bearing Duplex Stainless Steel. *Metals* **2019**, *9*, 930. [[CrossRef](#)]
26. Park, J.H.; Kang, Y. Inclusions in Stainless Steels—A Review. *Steel Res. Int.* **2017**, *88*, 1700130. [[CrossRef](#)]
27. Ha, H.Y.; Park, C.J.; Kwon, H.S. Effects of non-metallic inclusions on the initiation of pitting corrosion in 11% Cr ferritic stainless steel examined by micro-droplet cell. *Corros. Sci.* **2007**, *49*, 1266–1275. [[CrossRef](#)]
28. Ha, H.Y.; Park, C.J.; Kwon, H.S. Effects of misch metal on the formation of non-metallic inclusions and the associated resistance to pitting corrosion in 25% Cr duplex stainless steels. *Scr. Mater.* **2006**, *55*, 991–994. [[CrossRef](#)]
29. Newman, R. Pitting corrosion of metals. *Electrochem. Soc. Interface* **2010**, *19*, 33–38. [[CrossRef](#)]
30. Frankel, G.S. Pitting corrosion of metals a review of the critical factors. *J. Electrochem. Soc.* **1998**, *145*, 2186–2198. [[CrossRef](#)]
31. Ha, H.-Y.; Lee, T.-H.; Kim, S.-J. Role of nitrogen in the active-passive transition behavior of binary Fe–Cr alloy system. *Electrochim. Acta* **2012**, *80*, 432–439. [[CrossRef](#)]

